Inorganic Chemistry

Article

pubs.acs.org/IC

Fine Hierarchy of the V−O Bonds by Advanced Solid State NMR: Novel $Pb_4(VO_2)(PO_4)_3$ Structure as a Textbook Case

Grégory Tricot, Olivier Mentré, Sylvain Cristol, and Laurent Delevoye*

Université Lille Nord de France, CNRS UMR8181, Unité de Catalyse et de Chimie du Solide, UCCS USTL, F-59655 Villeneuve d'Ascq, France

Supporting Information

ABSTRACT: We report here a complete structural characterization of a new lead $Pb_4(VO_2)(PO_4)_3$ vanadophosphate compound by single crystal X-ray diffraction and ^{51}V and ^{31}P solid-state NMR spectroscopy. Although structural data are commonly used for the estimation of bond lengths and further delimitation of the true coordination number (e.g., octahedral: 6 versus 5 + 1 versus 4 + 2), we show here for the first time by solid-state NMR a more accurate appreciation of the V−O bonding scheme in this complex oxide which appears well adapted to the full series of vanado-phosphate materials. The direct characterization of V−O−P bridges through the J-mediated correlation $^{51}V\{^{31}P\}$ heteronuclear multiple quantum coherence (J-HMQC) technique allows a contrasted hierarchy of the V−O electronic delocalization and indirectly supports the presence or not of the V−O bond. In the reported lead vanado-phosphate structure, the two vanadium polyhedra that have been assigned to octahedra from a bond length point of view have been finally reclassified as tetra- and penta-coordinated units on the basis of the solid-state NMR results. More generally, we believe that the improved characterization of interatomic bonds in various vanado-phosphate structures by solid-state NMR will contribute to a better understanding of the structure/property relationships in this important class of materials.

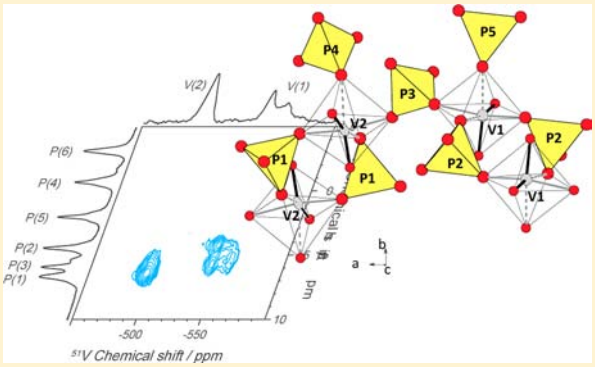

INTRODUCTION

From the structural viewpoint, vanadophosphate compounds give rise to a diversity of frameworks due to the combination of strong tetrahedral PO_4 connectors between VO_x polyhedra with versatile coordinations. Hence, it is admitted that pentavalent vanadium is able to adopt tetrahedral, square-pyramidal, trigonal-pyramidal, and distorted octahedral oxygen environments with V−O bonds in between 1.54 and 2.52 Å according to the bond classification developed in ref 1. This diversity of bonding schemes together with $[V_xO_y]$ units of variable dimensionalities (from 0D to 3D) articulated by phosphate ligands create structures with various dimensionalities eventually leading to porous frameworks.[1,2] In addition to V^{5+}, the stable $V^{3+}$and V^{4+} oxidation states extend all the more the diversification of possible structural archetypes. The number of compounds classified in the related chemical systems remarkably illustrates this structural richness.[1] As a matter of fact, the structural parameters driving the compound properties strongly depend on the coordination state of the vanadate sites and their versatile distribution of V−O bond lengths. In a simple approach, the bond strength is generally characterized by bond-valence calculations that correspond to an empirical estimation but often prevail for the deduction of the degree of covalency. Valuable information can also be derived from solid-state NMR. While the diffraction technique informs on the long-range order, NMR investigates the short-range order but is also capable of probing spatial proximity and chemical connectivity through the application of dipolar- or scalar-based sequences.

For the first time, we report that a rigorous combination of crystal-structure model and advanced NMR data allows the accurate establishment of the real VO_x bonding scheme. A meticulous analysis of the scalar-based $^{51}V/^{31}P$ NMR correlation spectrum allows for a contrasted hierarchy of the V−O electronic delocalization and indirectly supports the presence or not of the V−O orbital overlapping, leading to a detailed reclassification of the VO_n units. Of course, following the use of NMR spectroscopy, the current field of application of the developed methodology is only suitable for diamagnetic species, i.e. pentavalent vanadium cation.

This study has been performed on a novel vanadophosphate compound of formula $Pb_4(VO_2)(PO_4)_3$. The context of the evidence of this unreported phase is given in the supplementary data. Shortly, the new compound $Pb_4(VO_2)(PO_4)_3$ was evidenced during the investigation of the lead pyrovanadophosphate $Pb_2V_{2-x}P_xO_7$ system for the $x = 1.5$ composition. The crystal structure of the two end-members ($x = 0$ and 2) are similar and consist of X_2O_7 dimers with interstitial Pb^{2+} cations. However, for steric reasons, strong modifications of the

Received: May 10, 2012
Published: November 28, 2012

arrangements of the elementary XO_4 tetrahedra exist between both compounds at the origin of the symmetry and volume changes. The investigation of the V for P substitution in these two forms is analyzed by means of X-ray diffraction (XRD) and ^{31}P NMR spectroscopy on polycrystalline samples ($0 < x < 2$) prepared by solid state reaction. According to our results, it turns out that the vanadate form can accommodate up to 60% of phosphate ($x = 1.2$) while the phosphate form hosts up to 10% of vanadate ($x = 1.8$) within single-phased compound. For intermediate composition ($x = 1.5$), we observe the emergence of the $Pb_4(VO_2)(PO_4)_3$ phase. We assume that the ratio $x = 1.5$ represents a critical point for which the (P/V) average size is more adapted into a new structural arrangement with ordered V and P sites, rather than a statistical distribution in the structure of a pyro-like end-members. Such behavior is not unique, e.g. see the $BiCu_2(P_{1-x}V_x)O_6$ system for which intermediate modulated compounds ($0.6 \leq x \leq 0.9$) delimit a solid solution ($0 \leq x \leq 0.6$) and a commensurate supercell ordering ($x = 1$).[3] For $x = 1.5$, our profile fitting of XRD data shows only few impurity peaks which correspond to minor amount of the bordering $Pb_2V_{2-x}P_xO_7$ phase (Figure 2). An accurate determination of the P amount in each phases by ^{31}P NMR quantification shows that only 4% of the global phosphorus is present as an impurity (Figure S3a in the Supporting Information). The refined monoclinic lattice parameters are $a = 13.4945(2)$ Å, $b = 13.7944(2)$ Å, $c = 13.2713(2)$ Å, $\beta = 91.846(1)°$, $\chi^2 = 3.2\%$, $R_p = 7.62\%$, $R_{wp} = 11.6\%$. These data are in good agreement with the structure resolved by single-crystal XRD analysis presented in the next section, ($Pb_4(VO_2)(PO_4)_3$, CSD-number: 424267). The unit cell contains two independent distorted VO_6 sharing oxygen corners with five independent PO_4 groups within multiple connectivities. The local structure has been characterized by ^{51}V and ^{31}P 1D MAS NMR while the P−P and V−P interactions have been investigated by means of homonuclear and heteronuclear correlations using both dipolar (through-space) and scalar (through-bond) couplings, as further detailed.

EXPERIMENTAL SECTION

The new compound $Pb_4(VO_2)(PO_4)_3$ was evidenced during the investigation of the lead pyro-vanadophosphate $Pb_2V_{2-x}P_xO_7$ system for the $x = 1.5$ composition. Single crystals of that composition were obtained from a stoichiometric mixture of PbO, V_2O_5, and $(NH_4)_2H(PO_4)$ using a heating stage at 950 °C followed by a slow cooling process (3 °C/h). The polycrystalline samples have been prepared from the same batch composition with a heating stage at 700 °C for 48 h in Al_2O_3 crucibles, with several intermediate grindings. The crystal structure analysis certificates the nominal V/P = 1/3 ratio and the possibility to obtain single-phase powder material, by means of the XRD pattern simulation.

XRD Investigations. The purity of the powder have been checked by powder XRD using a D-5000 Bruker diffractometer, Cu Kα radiation. The single crystal data collection was performed using a SMART-Bruker CCD diffractometer. A full-Ewald sphere was collected using ω-scans. The absorption corrections were performed using the semiempirical method implanted in SADABS.[4a] Crystal structure was solved using the direct method with SHELXS[4b] and refined using JANA2000.[5]

NMR Investigations. ^{31}P and ^{51}V MAS NMR experiments were performed on a 400 WB Bruker spectrometer (9.4 T) operating at 161.9 and 105.2 MHz, respectively. All the NMR spectra were recorded at a spinning frequency (ν_{rot}) of 20 kHz using a 3.2-mm HXY probehead, except for the BABA spectrum which was recorded at ν_{rot} = 10 kHz on a 4-mm HXY probehead. The ^{51}V RA-MP decoupling conditions[6] (pulse length and interleaved delays in the Supporting Information) were optimized experimentally on the compound. It is important to remember that the RA-MP decoupling sequence was specially developed to remove broadening arising from scalar coupling with a quadrupolar nucleus. The *J*-HMQC (heteronuclear multiple quantum coherence) pulse sequence[7] is composed of an echo on the ^{51}V channel, modulated by two $\pi/2$ pulses on the ^{31}P channel, giving rise to scalar heteronuclear coherences. In the *D*-HMQC,[8] the heteronuclear dipolar interaction is reintroduced by the application of a recoupling sequence (SFAM for simultaneous frequency and amplitude modulation[9]) on the ^{31}P channel. In both *J*- and *D*-HMQC, central transition selective 90° and 180° pulses on ^{51}V were set to 22 and 44 μs, respectively, and ^{31}P 90° pulse to 2.7 μs. The ^{31}P and ^{51}V chemical shifts are referred to H_3PO_4 (85%) and $VOCl_3$, respectively. Other acquisition parameters are detailed in the Supporting Information.

RESULTS

Crystal Structure of the Novel $Pb_4(VO_2)(PO_4)_3$. The data for the single crystal XRD structural analysis and atomic, thermal parameters are given in Table 1. Multiscan types absorption corrections were applied to the raw data. The pertinent interatomic distances and the P−P and P−O−V connectivity scheme are reported in Table 2. The crystal structure is shown in Figure 1a projected along the *c*-axis. The two independent VO_6 octahedra share their corners with five of the six independent phosphate groups P(1) to P(5) to create a 3D porous framework. The created channels are hosted by an alternation of Pb^{2+} and $P(6)O_4$ tetrahedra as shown in Figure 1b. The XRD powder analysis of the $Pb_4(VO_2)(PO_4)_3$ is also given in Figure 2.

The building units that are forming the 3D framework are shown in Figure 1c. The vanadium oxygen coordinations are

Table 1. Crystal Data, Collection, and Refinement Parameters for the Structural Study of $Pb_2(PO_4)_{1.5}(VO_2)_{0.5}$

Crystal Data	
formula, Z, M_w(g)	$Pb_2(PO_4)_{1.5}(VO_2)_{0.5}$, 16, 598.32
symmetry	monoclinic
space group	$P2_1/c$
unit cell	a = 13, 493(4) Å
	b = 13, 798(4) Å, β = 91, 873(4)°
	c = 13, 274(4) Å
	V = 2470(1) Å^3
density (calc)	6.44
crystal size (μm)	140 × 60 × 20
Data Collection	
diffractometer	Bruker SMART CCD
λ Mo Kα (Å)	0, 7107
scan type	ω-scan
explored reciprocal space	$-18 \leq h \leq 18$, $-18 \leq k \leq 18$, $-17 \leq l \leq 18$
$\theta_{min}/\theta_{max}$ (deg)	3.07/29.40
no. measured reflexions	18920
no. ind reflexions, $N > 2\sigma(I)$	6093, 3850
R_{int} (%), 2/*m* Laue class	10.96
Refinement	
software, method	SHELXL, least-squares on F^2
no. ref param./constraints	258/0
anisotropic thermal param.	all Pb, V, and P atoms
R_1 (%)	9.9 (all)/6.3 ($I > 2\sigma(I)$)
wR_2 (%)	13.6 (all)/12.6 ($I > 2\sigma(I)$)
GooF	0.946
ρ_{max}/ρ_{min} (e$^-$·Å^{-3})	8.104/−7.845

dx.doi.org/10.1021/ic300966r | Inorg. Chem. 2012, 51, 13108−13113

Table 2. (a) P−P Interatomic Distances (Å), (b) V−O−P Connectivity Scheme, and (c) V−P, V−O, and O−P Interatomic Distances with Bond Valence Sum Calculations for $Pb_4(VO_2)(PO_4)_3$

(a)	P(1)	P(2)	P(3)	P(4)	P(5)	P(6)
P(1)	4.408	5.862	5.060	5.162	4.797	4.476
P(2)		4.501	5.146	4.949	5.243	4.694
P(3)			>6	4.500	4.278	5.986
P(4)				4.448	>6	4.741
P(5)					4.631	4.868
P(6)						>6

(b)	P(1)	P(2)	P(3)	P(4)	P(5)	P(6)
V(1)	0	2	1	0	1	0
V(2)	2	0	1	1	0	0

(c) V−O−P	V−P (Å)	V−O (Å)	O−P (Å)	$S_{(V-O)}$
V(1)−O(9)−P(2)	3.391	2.196	1.512	0.34
V(1)−O(18)−P(2)	3.183	1.942	1.547	0.69
V(1)−O(19)−P(3)	3.364	2.009	1.560	0.57
V(1)−O(11)−P(5)	3.441	2.132	1.527	0.41
V(1)−O(10)		1.636		1.57
V(1)−O(16)		1.624		1.62
			$\sum S_{ij}$ = 5.20	
V(2)−O(4)−P(1)	3.167	2.101	1.527	0.45
V(2)−O(8)−P(1)	3.149	1.909	1.544	0.75
V(2)−O(7)−P(3)	3.339	2.017	1.544	0.56
V(2)−O(12)−P(4)	3.723	2.300	1.555	0.26
V(2)−O(15)		1.585		1.80
V(2)−O(23)		1.713		1.27
			$\sum S_{ij}$ = 5.09	

presented on the basis of short (1.54 < V^V−O < 1.75 Å), intermediate (1.84 < V^V−O < 2.06 Å), and long (2.13 < V^V−O < 2.52 Å) V−O bonds, according to the empirical classification by Boudin et al.[1] At first sight, both the V(1) and V(2) sites can be described as 2 + 2 + 2 distorted octahedra. However, V(2)−O(4) = 2.101(13) Å falls right between the "long" and "intermediate" empirical ranges and its real bonding nature is questionable. These data demonstrate the actual limit of the bond-length nomenclature that fails here. It follows that bond valence sum analysis (see Table 1c) also gives a poor image of the degree of orbital overlapping/covalent character since S_{ij} take values that range from weak to strong contributions directly related to the concerned V−O distances.

NMR Characterization. *P/V Attribution from 1D and Homonuclear Correlation NMR Spectra.* The ^{31}P MAS NMR spectra acquired under and without ^{51}V-decoupling conditions are reported in Figure 3a and b, respectively. The ^{51}V-decoupled acquisition reveals the presence of six major P-contributions in equal proportions at −3.2, −0.8, 1.9, 4.3, 5.9, and 6.6 ppm, in a good agreement with the crystallographic data. It is noticeable that only the three resonances at 6.6, 5.9, and 4.3 ppm are greatly affected by the decoupling (Figure 3a), suggesting that these sites are involved in a strong scalar coupling with vanadate species. In addition to the six major contributions, the presence of weak impurities is observed at 5.4 ppm.

The 2D ^{31}P BABA[10] NMR spectrum (Figure 3c) shows spatial proximity between (i) equivalent P sites through on-diagonal signals and (ii) nonequivalent P sites through off-diagonal correlation signals. The spectrum displays correlation signals between all phosphorus sites, separated by less than 6 Å.

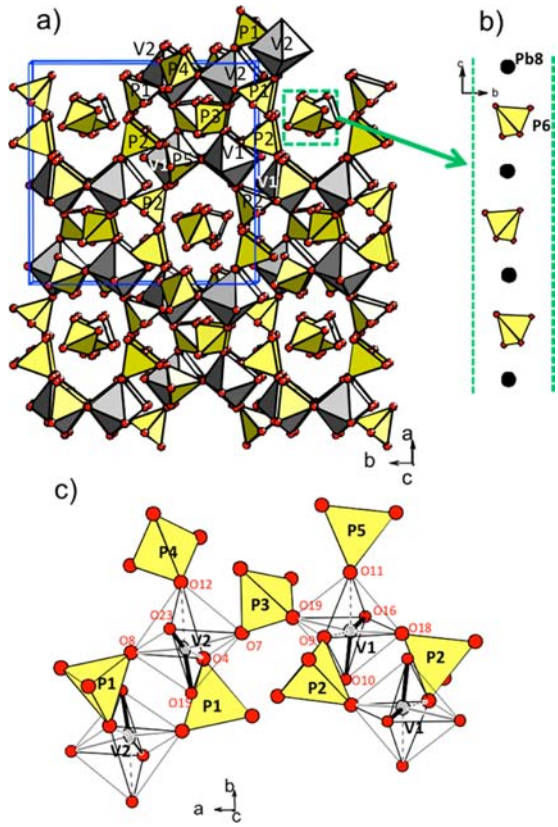

Figure 1. (a) 3D porous network in the absence of the Pb^{2+} cations. Yellow and white polyhedral stand for PO_4 and VO_6 units. (b) Evidence of Pb(8) and P(6)O_4 in the channels growing along the *c*-axis. (c) Bonding scheme between PO_4 and VO_6 polyhedra. In the latter figure, solid-black, solid-gray, and dotted-gray bonds stand for short, intermediate, and long V−O bonds according to the classification developed in ref 1.

The absence of on-diagonal signal at 5.9 and −3.2 ppm (squares), associated with the unequivocal presence of V−P scalar coupling for the former site and the connectivity scheme reported in Table 2b, assign the two resonances to the P(3) and P(6) crystallographic sites, respectively. For similar distance considerations, the missing off-diagonal signal at 1.9 and −0.8 ppm sites (circles) corresponds to the [P(4), P(5)] pair (Table 2). However, the attribution of these two sites cannot be achieved exclusively on the basis of the homonuclear correlation data.

The 1D ^{51}V MAS NMR spectrum is shown in Supporting Information Figure S3b. As expected from the structure, two signals are observed, one with a typical line broadening from the second-order quadrupolar interaction.[11] The ^{51}V MAS NMR assignment derives from the calculation of the quadrupolar parameters reported in Supporting Information Table S3b. Experimentally, the vanadium sites exhibit different C_Q values, respectively 4.7 and 7.5 MHz, as estimated from the MAS spectrum. The comparison of the experimental C_Q with those deduced from the DFT calculations allow assigning the NMR signals at −525 ppm, showing the large electric field gradient, to V(1) and the site at −489 ppm to V(2).

Final Assignment from Heteronuclear Correlation Spectra. The 2D ^{51}V{^{31}P} *D*-HMQC spectrum is reported in Figure 4b along with ^{51}V projection (top spectrum). The spatial proximity between vanadate and phosphate species is highlighted by the presence of several correlation signals. The 2D spectrum clearly

dx.doi.org/10.1021/ic300966r | *Inorg. Chem.* 2012, 51, 13108−13113

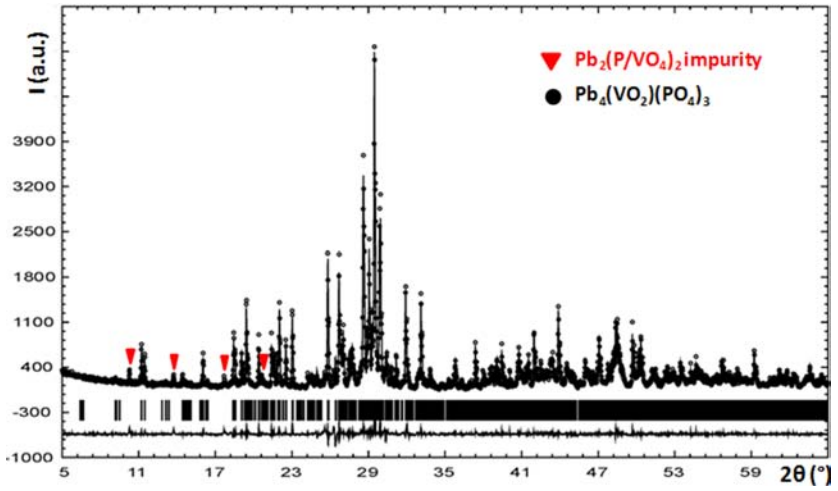

Figure 2. Profile-fitting XRD powder analysis of the $Pb_4(VO_2)(PO_4)_3$ sample.

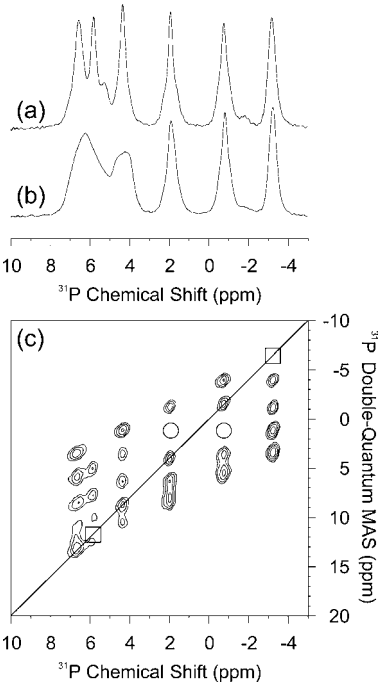

Figure 3. ^{31}P MAS NMR spectra of $Pb_4(VO_2)(PO_4)_3$ obtained by single pulse with (a) and without (b) ^{51}V RA-MP decoupling.[6] (c) ^{31}P 2D double quantum spectrum obtained with the BABA sequence.[10] Circles and squares highlight the absence of correlation signals.

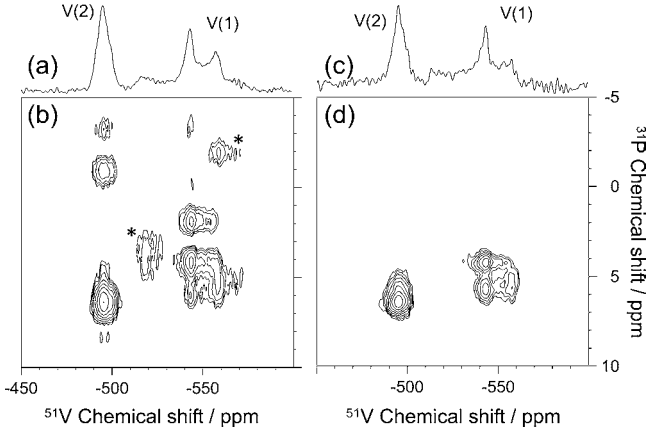

Figure 4. ^{51}V MAS NMR projections of the *D*-HMQC (a) and *J*-HMQC (c) spectra with corresponding assignment. 2D Correlation spectra using the $^{51}V\{^{31}P\}$ *D*-HMQC[8] (b) and *J*-HMQC[7] (d) sequences. Asterisks indicate the presence of impurities.

indicates spatial proximity between V(1) and phosphorus sites at 5.9, 4.3, and 1.9 ppm, on one hand and between V(2) and phosphorus sites at 6.6, 5.9, and −0.8 ppm on the other hand. The final assignment was performed as follows:

(i) The phosphorus site at 5.9 ppm clearly shows correlation signals with both vanadium sites confirming its assignment to P(3). Very low intensity signals are observed between the −3.2 ppm site and both vanadium sites, supporting its assignment to P(6) in good agreement with the long V(1/2)-P(6) distances (>5 Å).

(ii) The proximity of V(2) and phosphorus site at −0.8 ppm as well as the proximity of V(1) and the phosphorus site at 1.9 ppm allows completing the assignment of P(4) and P(5) at respective chemical shifts (Table 2b).

(iii) Finally, the sites at 6.6 and 4.3 ppm are assigned to P(1) and P(2), respectively, accordingly to the V(2)−P(1) and V(1)−P(2) connectivities (Table 2b). It is noteworthy that the low-field evolution of the ^{31}P chemical shift occurring when the number of connected vanadium increases is in line with previous results obtained on crystalline or amorphous vanadophosphate materials.[12−15]

The complete ^{31}P signal assignment is reported in Supporting Information Table S3b. Figure 4d depicts the 2D $^{51}V\{^{31}P\}$ *J*-HMQC showing the heteronuclear correlation via the scalar coupling. The structural information deduced from this spectrum clearly confirms the previous assignment, i.e. P(1) at 6.6, P(3) at 5.9, and P(2) at 4.3 ppm, with rough similarity between spatial proximity and chemical bonding for V(1)−P(2), V(1)−P(3), V(2)−P(1), and V(2)−P(3). However, clear differences appear in the *J*-HMQC spectrum that does not exhibit any V−P correlation signal associated with the 1.9 ppm (P(5)) and −0.8 ppm (P(4)) sites despite significant V(1)−O(11)−P(5) and V(2)−O(12)−P(4) connectivities (Table 2). A ^{51}V transverse relaxation T_2' of 24 ms has been measured experimentally (Supporting Information Figure S3d). In any case, the absence of correlation could not be explained

dx.doi.org/10.1021/ic300966r | Inorg. Chem. 2012, 51, 13108−13113

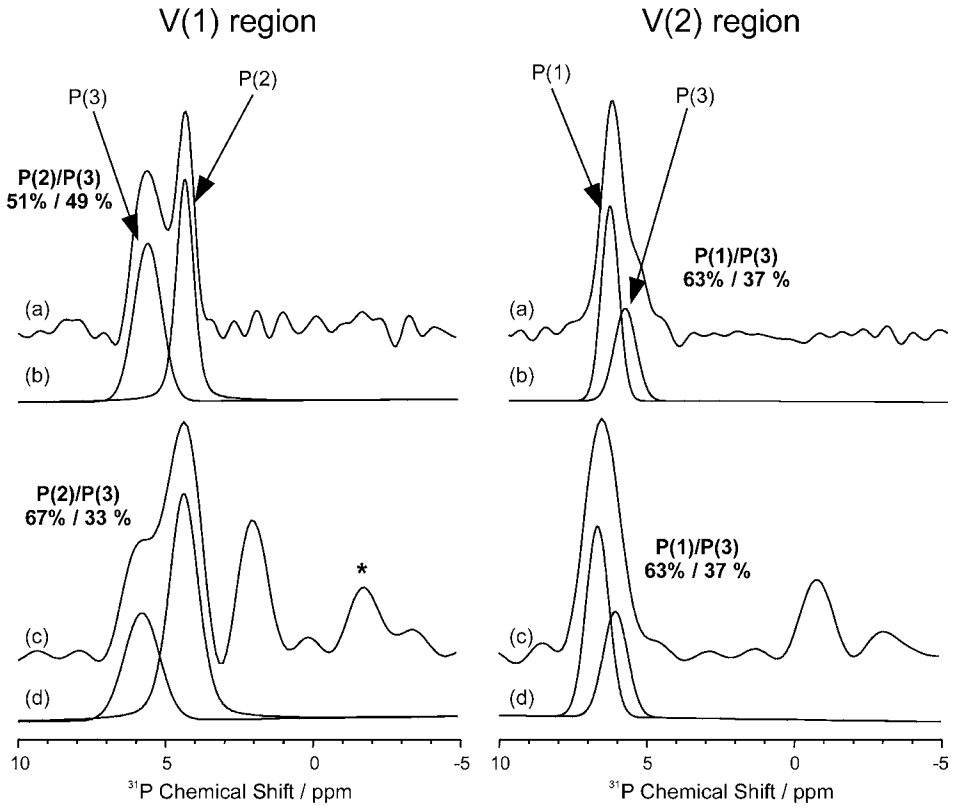

Figure 5. ^{31}P MAS projections from selected regions of the *J*-HMQC (a) and *D*-HMQC (c) correlation spectra. The V(1) and V(2) regions were obtained by summation of the 2D data for chemical shifts in between [−530; −580 ppm] and [−485; −505 ppm], respectively. Each projection spectrum is shown with the corresponding best-fit simulation in b and d with the relative ratio of phosphorus sites in the region [3; 7 ppm].

by short ^{51}V transverse relaxation times, since the T_2' values for V(1) and V(2) are sufficient to observe correlations with P(1), P(2), and P(3), in the lower part of the spectrum. The *J*-HMQC build-up curve (Supporting Information Figure S3e), giving a maximum signal at 10 ms, has been fitted to evaluate the $^2J(^{31}P-O-^{51}V)$ scalar couplings to about 40 Hz. The difference between the *D*- and *J*-HMQC spectra results from structural considerations to be addressed in the following section. It is noteworthy that the *J*-HMQC results have been confirmed by the correlation spectrum obtained with the scalar-mediated $^{31}P\{^{51}V\}$ INEPT technique (Supporting Information Figure S3c).

DISCUSSION

V−O Bonding Classification. The qualitative analysis of the ^{51}V decoupling of the ^{31}P MAS NMR spectrum (Figure 3a) together with the *J*-HMQC correlation spectrum brings a contrasted view of the coordination of vanadium sites. On the one hand, the *J*-HMQC spectrum of $Pb_4(VO_2)(PO_4)_3$ shows no correlation signal for P(6) (no V−P connectivity) and for P(4) and P(5), characterized by long V−O distances (V(2)−O(12)−P(4): V−O = 2.30 Å and V(1)−O(11)−P(5): V−O = 2.13 Å). For P(4) and P(5), it reveals small scalar coupling with surrounding vanadium. On the other hand, a significant correlation exists for P(3), via V−O bonds (e.g., V(2)−O(7)−P(3): V−O = 2.02 Å). Thus, the absence of these correlations based on the *J* coupling, for V−O bonds greater than 2.13 Å, allows an accurate boundary to be drawn between predominating covalent or not V−O bridges. Here, within the V−O−P path, our methodology considers fully homogeneous PO_4 groups with similar covalency over the four P−O distances. In other words, slight deviations in terms of distances from one P−O to another are not considered. Clearly, a most accurate hierarchy of V−O bonds within the empirical short-/intermediate-/long- nomenclature[1] is allowed.

An even more accurate boundary can be drawn through the close analysis of the P−V correlations for all independent P sites. Especially the V(1)−P(2) and V(2)−P(1) connectivities being multiple, i.e. V(1)−O(9)−P(2): V−O = 2.20 Å vs V(1)−O(18)−P(2): V−O = 1.94 Å, and V(2)−O(4)−P(1): V−O = 2.10 Å vs V(2)−O(8)−P(1): V−O=1.91 Å, it is worth estimating each individual V−O contribution. Thus, we have extracted the P−V(1) and P−V(2) contributions from the 2D *D*-HMQC and *J*-HMQC correlation maps. Around V(1) (Figure 5, left), only the *D*-HMQC correlation pattern exhibits the expected 2:1 intensity ratio in agreement with the vicinity of two P(2) and one P(3) neighbors. As expected, the *J*-HMQC projection displays a 1:1 relative weight for P(2)/P(3), thus confirming the absence of contribution from the long V(1)−O bond. For the V(2) environment (Figure 5, right), both *D*- and *J*-HMQC projections can be best fitted with two sites P(1)/P(3) in a relative ratio of ca. 2:1. This means that P(3)−O−V(2) and each P(1)−O−V(2) paths equally contribute to the *J*-HMQC signal, including the longer V(2)−O(4) bond of 2.10 Å. From our experimental data set, the 2.10 to 2.13 Å V−O range appears to be the critical zone at the frontier of observable or not scalar coupling. It is clearly related with the degree of covalence of the concerned *J* paths and pictures the real chemical bonding. In the title compound, accordingly to the bond-mediated NMR data, V(1) should be better considered as a distorted octahedron with a true tetra-

dx.doi.org/10.1021/ic300966r | *Inorg. Chem.* 2012, 51, 13108−13113

coordination, 2 + 2(+2), while V(2) corresponds to a even more distorted octa-coordinated polyhedron, 2 + 3(+1).

CONCLUSION

We have demonstrated here the efficiency of 2D $^{51}V\{^{31}P\}$ *J*-HMQC scalar coupling to distinguish the real V−O bonding scheme in a much more accurate way than the standard bond valence concept. In the investigated $Pb_4(VO_2)(PO_4)_3$, the two vanadium atoms obey an unified classification in terms of V−O bond length versus the mediating J-coupling, i.e. V−O distances above 2.13 Å do not present a significant covalent character. Indeed, at first sight both studied VO_6 octahedra present comparable distribution of short, medium, and long bond lengths. In fact, the bond strength also depends on the distribution of V−O bond length around the central V^{5+}. Then, the investigation of further materials with various P−O−V topologies should give additional clues toward a more extended unified panorama. At least, for the first time, to our knowledge, we provide a reliable estimation of the chemical bond strength, giving new insight into the real vanadium−oxygen coordination. We believe that this kind of hierarchy is of a crucial importance to clearly establish the property/structure relationships, at least in the important class of vanadophosphate materials. At this point, it is clear that the interest of phosphorus for V−P couplings spectroscopy is multiple: (i) PO_4 groups are generally regular tetrahedral, meaning that the four P−O bonds are of comparable strength. It follows that V−P scalar couplings indirectly probes the V−O contribution in all situations. (ii) Owing to its NMR characteristics (100% natural abundance and high sensitivity), ^{31}P nucleus allows for the acquisition of high quality data for detailed analysis, within reasonable measuring times. Finally, recent progress in NMR methodology allows viewing a diversification of the pertinent chemical systems toward an extended range of nuclei and heteronuclear correlation methods, beyond the phosphorus−vanadium class of materials.

ASSOCIATED CONTENT

Supporting Information

Crystallographic data in Tables S1 and XRD patterns and lattice parameters for the $Pb_2V_{2-x}P_xO_7$ system in Figure S1. Details about the DFT calculations of ^{51}V quadrupolar parameters and further information about NMR acquisitions. Best-fit simulation of the ^{31}P MAS NMR spectrum in Figure S3a with results in Table S3a. The ^{51}V MAS NMR spectrum in Figure S3b, the ^{51}V NMR parameters and ^{31}P assignment in Table S3b, and the $^{31}P\{^{51}V\}$ INEPT spectrum in Figure S3c. Figures S3d and S3e provide an estimation of ^{51}V T_2' transverse relaxation and $^{51}V-^{31}P$ scalar coupling, respectively. This material is available free of charge via the Internet at http://pubs.acs.org.

AUTHOR INFORMATION

Corresponding Author

*E-mail: laurent.delevoye@ensc-lille.fr.

Notes

The authors declare no competing financial interest.

ACKNOWLEDGMENTS

The "Fonds Européen de Développement Régional (FEDER)", "CNRS", "Région Nord Pas-de-Calais", and "Ministère de l'Education Nationale de l'Enseignement Supérieur et de la Recherche" are acknowledged for fundings of X-ray and NMR equipment.

REFERENCES

(1) Boudin, S.; Guesdon, A.; Leclaire, A.; Borel, M. *Int. J. Inorg. Mat.* **2000**, *2*, 561−579.
(2) Riou, D.; Férey, G. *J. Solid State Chem.* **1994**, *111*, 422−426.
(3) Leclaire, A.; Borel, M.; Chardon, J.; Raveau, B. *Solid State Sci.* **2000**, *2*, 293−297.
(4) (a) Sheldrix, G. *SADABS: Area-Detector Absorption Correction*; Siemens Industrial Automation, Inc.: Madison, WI, 1996. (b) Sheldrix, G. *SHELXTL package*; Bruker Analytical X-ray Systems, Madison, WI, 1997.
(5) Sheldrix, G.; Petricek, V.; Dusek, M. *The crystallographic computing system JANA2000*; Institute of Physics, Praha, 2000.
(6) Delevoye, L.; Trébosc, J.; Gan, Z.; Montagne, L.; Amoureux, J.-P. *J. Magn. Reson.* **2007**, *186*, 94−99.
(7) Lesage, A.; Sakellariou, D.; Steuernagel, S.; Emsley, L. *J. Am. Chem. Soc.* **1998**, *120*, 13194−13201.
(8) Tricot, G.; Lafon, O.; Trébosc, J.; Delevoye, L.; Mear, F.; Montagne, L.; Amoureux, J. P. *Phys. Chem. Chem. Phys.* **2011**, *13*, 16786−16794.
(9) Fu, R.; Smith, S. A.; Bodenhausen, G. *Chem. Phys. Lett.* **1997**, *272*, 361−369.
(10) Schnell, I.; Brown, S. P.; Low, H. Y.; Ishida, H.; Spiess, H. W. *J. Am. Chem. Soc.* **1998**, *120*, 11784−11795.
(11) Ashbrook, S. E. *Phys. Chem. Chem. Phys.* **2009**, *11*, 6892−6905.
(12) Huang, W.; Vega, A. J.; Guillon, T.; Polenova, T. *J. Am. Chem. Soc.* **2007**, *129*, 13027−13034.
(13) Eichele, K.; Grimmer, A.-R. *Can. J. Chem.* **2011**, *89*, 870−884.
(14) Hudalla, C.; Eckert, H.; Dupree, R. *J. Phys. Chem.* **1996**, *100*, 15986−15991.
(15) Tricot, G.; Montagne, L.; Delevoye, L.; Palavit, G.; Kostoj, V. *J. Non-Cryst. Solids* **2004**, *345−346*, 56−60.